Transfer of Macroscale Tissue Strain to Microscale Cell Regions in the Deformed Meniscus

Maureen L. Upton,* Christopher L. Gilchrist,* Farshid Guilak,*† and Lori A. Setton*†
*Department of Biomedical Engineering, Duke University, Durham, North Carolina; and †Division of Orthopaedic Surgery, Department of Surgery, Duke University Medical Center, Durham, North Carolina

ABSTRACT Cells within fibrocartilaginous tissues, including chondrocytes and fibroblasts of the meniscus, ligament, and tendon, regulate cell biosynthesis in response to local mechanical stimuli. The processes by which an applied mechanical load is transferred through the extracellular matrix to the environment of a cell are not fully understood. To better understand the role of mechanics in controlling cell phenotype and biosynthetic activity, this study was conducted to measure strain at different length scales in tissue of the fibrocartilaginous meniscus of the knee joint, and to define a quantitative parameter that describes the strain transferred from the far-field tissue to a microenvironment surrounding a cell. Experiments were performed to apply a controlled uniaxial tensile deformation to explants of porcine meniscus containing live cells. Using texture correlation analyses of confocal microscopy images, two-dimensional Lagrangian and principal strains were measured at length scales representative of the tissue (macroscale) and microenvironment in the region of a cell (microscale) to yield a strain transfer ratio as a measure of median microscale to macroscale strain. The data demonstrate that principal strains at the microscale are coupled to and amplified from macroscale principal strains for a majority of cell microenvironments located across diverse microstructural regions, with average strain transfer ratios of 1.6 and 2.9 for the maximum and minimum principal strains, respectively. Lagrangian strain components calculated along the experimental axes of applied deformations exhibited considerable spatial heterogeneity and intersample variability, and suggest the existence of both strain amplification and attenuation. This feature is consistent with an in-plane rotation of the principal strain axes relative to the experimental axes at the microscale that may result from fiber sliding, fiber twisting, and fiber-matrix interactions that are believed to be important for regulating deformation in other fibrocartilaginous tissues. The findings for consistent amplification of macroscale to microscale principal strains suggest a coordinated pattern of strain transfer from applied deformation to the microscale environment of a cell that is largely independent of these microstructural features in the fibrocartilaginous meniscus.

INTRODUCTION

Mechanical signals play important roles in regulating cell viability, differentiation, and extracellular matrix (ECM) synthesis and organization in musculoskeletal and connective tissues, including articular cartilage, the fibrous tendon and ligament, and the fibrocartilaginous intervertebral disc and meniscus (1,2). It is known, however, that these tissues exhibit dramatically diverse biological responses to well controlled mechanical loading regimens (3–6). These cellular responses may vary not only across tissue types (3) but also within each tissue in manners that depend on numerous factors, including the loading mode and duration (i.e., tension, compression, and shear) (3,5–7), frequency (5,8), and magnitude (5,9), as well as the anatomic regional location of the cells (5,7,10). These observations result, in part, from the existence of numerous types of mechanical stimuli at the immediate vicinity or microenvironment of a resident cell, including hydrostatic pressures, fluid flow, compressive and tensile stress and strain, and volumetric changes that can independently or simultaneously result from a well controlled loading regimen (5,11–16). Numerous interactions can occur among structures of the ECM in response to physical loading, such as conformational changes, molecular sliding, formation and breakage of molecular linkages, that contribute to these variable states of mechanical stimuli within three-dimensional, extracellular matrices. However, limited information is available on the relationship between an applied mechanical stimulus and the resulting spatial variations in magnitude and sense of mechanical stimuli within the cell's microenvironment. Understanding these links between applied mechanical factors and locally induced physical stimuli will provide new insights regarding the role of mechanics in regulating tissue-specific biosynthesis and cell phenotype, as well as for designing appropriate repair strategies.

There is great interest in new methodologies that can elucidate the relationship between mechanics at the length scale of a cell as compared to those at the length scale of the far-field ECM (17,18). Recent experimental studies have investigated the relationship between these matrix-level mechanics and mechanical stimuli in the cell microenvironment using cells in material scaffolds, or cells interacting with material or tissue surfaces (19–26). Within the three-dimensional matrix of articular cartilage, volume changes and axial strain applied to the tissue have been shown to correlate with axial strain and volumetric changes for the embedded cells, or chondrocytes,

Submitted December 1, 2007, and accepted for publication April 24, 2008.

Address reprint requests to Lori A. Setton, PhD, Dept. of Biomedical Engineering, 136 Hudson Hall, Duke University, Durham, NC 27708. Tel.: 919-660-5131; Fax: 919-681-8490; E-mail: setton@duke.edu.

Editor: Richard E. Waugh.

0006-3495/08/08/2116/09 $2.00

doi: 10.1529/biophysj.107.126938

using fluorescent cell labeling in conjunction with laser scanning confocal microscopy, three-dimensional geometric rendering techniques, or digital image correlation (21,22,24). These studies illustrate that native cells within articular cartilage experience kinematic features of strain and dilatation that correspond to the sense of strain in their ECM, in a pattern that varies among the surface, middle, and deep zones of the tissue layer (22). In more-fibrous tissues, the physical processes of transducing deformation, strain, displacement, or volume change to the microenvironment of the cell appear more variable. In tissues such as tendon and the fibrous region of the intervertebral disc, or anulus fibrosus (19,20,27,28), a spectrum of ''microscale'' tissue and cell deformation behaviors have been reported that do not scale in magnitude or directly correlate with mechanical stimuli applied to the tissue explant. Examples include findings of local strain measurements that are significantly less than the applied macroscale or grip-to-grip strain, mean intercellular strains close to zero, and microscale strains that vary in sense from the applied deformation (19,20,27,28). In fibrous tissues, some of these phenomena may be attributed to collagen fiber sliding and recruitment at the level of the microscale or cellular length scale (20,28). Furthermore, fibrous and fibrocartilaginous tissues (such as tendon and anulus fibrosus) exhibit significant heterogeneity in matrix microstructure because of the presence of fiber bundles that are known to intertwine, terminate, or vary in diameter across very localized spatial regions (29,30). Thus, the variable findings reported for strain transfer in fibrocartilaginous tissues likely reflect morphologically distinct tissue subregions, and these heterogeneous results are difficult to resolve by measuring, e.g., intercellular distances. Few studies, however, have measured kinematic variables at multiple length scales, or in more than one direction, to determine whether applied tissue-level mechanical stimuli directly relate to mechanics within the cellular microenvironment.

For this study, we investigated the link between tissue length scale and microscale mechanics in the knee joint meniscus. The knee joint meniscus is a heterogeneous fibrocartilaginous tissue with morphological, load-bearing, and biochemical features similar to those of the fibrous ligament and tendon, as well as articular cartilage. Cells of the meniscus reside and interact with the dense and highly organized yet spatially heterogeneous ECM, which is composed of a mixture of aligned types I and II collagen fiber bundles and glycosaminoglycans (31–35). Meniscus cells regulate their biosynthesis and gene expression in response to altered mechanical stimuli in vivo (36–38), compressive loading of explants in vitro (4,6,10,39), and tensile stimuli of cells in monolayer culture (40,41). Although the cells are clearly responsive to mechanical stimuli in their environment, the precise magnitude, sense, and temporal pattern of these stimuli are as uncertain in the meniscus as in other fibrochondrocytic cells. With its highly oriented fibrillar network, the meniscus is a model fibrocartilage for studying the transfer of applied mechanical loads to local mechanical stimuli in the vicinity of an embedded cell. This study investigated the biological problem of strain transfer to a microenvironment consisting of a cell and its immediate matrix using experimental methods in optics and solid mechanics.

The objective of this study was to measure strain at different length scales in tissue explants of the meniscus, and to develop a quantitative parameter that represents the transfer of strain from the far-field ECM to the local cellular microenvironment. The motivating hypothesis was that the far-field tissue strain would correspond in sense and magnitude to that transferred to the local, microenvironment of all resident cells. In this study, a controlled displacement representing uniaxial tensile deformation was applied to explants of porcine meniscus using a custom-designed device, and two-dimensional strain fields were measured in the ''macroscale'' ($\sim$1 mm) and ''microscale'' ($\sim$0.1 mm) using fluorescence matrix labeling, confocal microscopy, and texture correlation analysis. These length scales were chosen to represent the far-field tissue and the cellular microenvironment. A strain transfer ratio (STR) was calculated as a measure of the correspondence between micro- and macroscale strains in the ECM induced by the applied tensile deformation.

MATERIALS AND METHODS

Meniscus sample preparation

Porcine menisci ($n = 12$, procured from a local abattoir) were harvested from skeletally mature knee joints within 6 h of sacrifice. One or two slab-shaped tissue explants (25–30 $\times$ 2.5–4 $\times$ 2–3.5 mm, length $\times$ width $\times$ thickness) were obtained from the radially outer region (2–6 mm from the peripheral rim) in the circumferentially central zone of each meniscus (i.e., not near anterior or posterior horns). The explants were prepared such that the macroscopically aligned collagen fibers in the sagittal plane were oriented along the explant length. After harvest, explants were placed in culture medium (DMEM containing 10% FBS, 1% HEPES, 1% nonessential amino acids, 37.5 μg/mL ascorbate-2-phosphate, 100 U/mL penicillin, and 100 μg/mL streptomycin; Sigma Chemical, St. Louis, MO) for 24–48 h before the deformation experiment.

On the day of the experiment, explants were washed twice in D-PBS (Invitrogen, Carlsbad, CA) for 3 min and incubated in series with freshly diluted fluorescent dyes appropriate for labeling either the cells (SYTO82, 2 μM final concentration in D-PBS, 90 min, 37°C; Invitrogen) or the ECM (dichlorotriazinylamino fluorescein (DTAF), 2 mg/mL in 0.2 M sodium bicarbonate buffer pH 9.0, 15 min, room temperature; Invitrogen), followed by washing to remove residual DTAF (2$\times$ for 3 min each with sodium bicarbonate buffer). DTAF was used as a general protein stain to label primary amines in the ECM and to reveal heterogeneities in ECM morphology. This staining method illustrated several distinct patterns of matrix organization using microscopic imaging, as depicted in Fig. 1. Meniscus cells appeared to reside within regions characterized by one of the following ECM descriptors: 1), aligned collagen fibers or fiber bundles as identified by a distinct crimping pattern; 2), uniform or homogeneously organized matrix with few fibrous features; 3), terminating fibrous structures, identified by semicircular patterns that appear contiguous to each other denoted as ''fiber junctions''; and 4), discontinuous and more punctate stained matrix with no identified aligned fibers, defined here as ''nonfibrous'' matrix. These classifications were meant to be descriptive of ECM features, and no further quantitation of

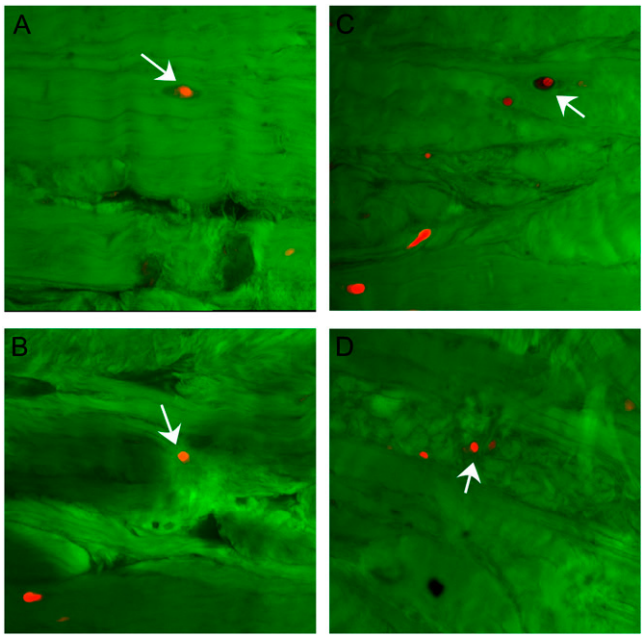

FIGURE 1 Images depict representative cellular interactions with the ECM in the meniscus. The ECM is labeled green by DTAF staining and all cells appear as red circles or a combination of a red circle surrounded by a circular or oval shape of low-intensity stained pixels, indicating exclusion of the DTAF molecule from the cell cytoplasm. The cell of interest in each panel is denoted by a white arrow. The meniscus cell appears embedded within (*A*) aligned collagen fibers, (*B*) in the middle of a fiber junction, (*C*) homogeneously stained and organized ECM, and (*D*) in nonfibrous matrix.

matrix structure was performed. Cells and matrix were imaged in all of these possible tissue regions for determination of microscale strains as described below.

Custom tissue deformation device and experimental setup

For each experiment, meniscus samples were deformed in uniaxial tension. The meniscus explant was placed into two test grips (Fig. 2) and assembled into a custom-designed deformation device to permit visualization of the sample. The deformation device consisted of a linear slide (CR4501; Daedel Positioning, Irwin, PA) and a micrometer (BM25.40; Newport, Irvine, CA) to apply displacements to the tissue samples, which were assembled on top of a baseplate with a recessed chamber. The chamber was designed to hold fluid and to allow for visualization of a tissue explant through a coverslip flush with the chamber surface. The baseplate interfaced directly with the *x-y* motorized stage (Scan IM; Marzhauser, Wetzlar-Steindorf, Germany) of an inverted confocal microscope (LSM 510; Carl Zeiss, Jena, Germany). The meniscus sample was allowed to equilibrate within the grips and device in a bath of sodium bicarbonate for 30 min before deformation.

Microscopic imaging of sample deformations

Fields of view (FOVs) were identified to measure strain at the macroscale corresponding to the far-field tissue (i.e., 10× magnification, 921.4 μm × 921.4 μm), and at the microscale corresponding to microenvironments (i.e., 40× magnification, 230.3 μm × 230.3 μm) in the vicinity of an observed cell, termed the ''cell microenvironment.'' These FOVs were identified by visualizing fluorescence generated by DTAF staining of the ECM and SYTO82-labeled cells. Within the identified 10× FOV, three to four discrete microscale FOVs at 40× magnification were identified, and subregions of these microscale FOVs were used to measure strain in the cell microenvironment. Because cell microenvironments contain both a cell and surrounding matrix, the spatially varying microscale strain reported represents a continuous strain field across both cell and the neighboring ECM. Thus, an average microscale strain does not represent cellular strain, but rather the average strain in the smaller FOV representing the cell and its immediate microenvironment.

Two-dimensional (512 × 512 pixels) 12-bit images were acquired consecutively of the reference, or undeformed, state at 10× (slice thickness = 31.2 μm) and at each 40× magnification (slice thickness = 3.16 μm). All images were acquired using multichannel imaging where one channel represented the cells (SYTO82, excitation with 543 nm, emission LP 585 nm) and one channel represented the labeled ECM (DTAF, excitation with 488 nm, emission BP 505–550 nm). After acquisition of the reference images, the meniscus explant was subjected to tensile displacement corresponding to increments of 1.5% grip-to-grip tensile strain ($\varepsilon_{applied}$) along the *x* axis, whereas the transverse direction (*y* axis) of the tissue remained unconstrained. Each incremental strain was consistently applied over 1 min to visually track the target 10× field of view (FOV). Two-dimensional images and three-dimensional image stacks were acquired of all identified FOVs at 10× and 40× after each strain increment, to represent the deformed state. To capture equilibrium strain values, images were acquired at no less than 5 min after deformation; this time point was chosen based on preliminary studies that showed minimal changes in median strain values or load cell readings after this time. A total of three or four tensile strain increments were applied to each sample, which resulted in a maximum $\varepsilon_{applied}$ between 4.5% and 6%. These magnitudes represent an expected physiologic level of tensile strains in the meniscus based on finite element models (16).

Strain field calculations with texture correlation analysis

Texture correlation analysis is a subset of digital image correlation that tracks the displacement of a grid of points in an image pair, which can be used to calculate strain (42). Texture correlation analysis assumes that each pixel

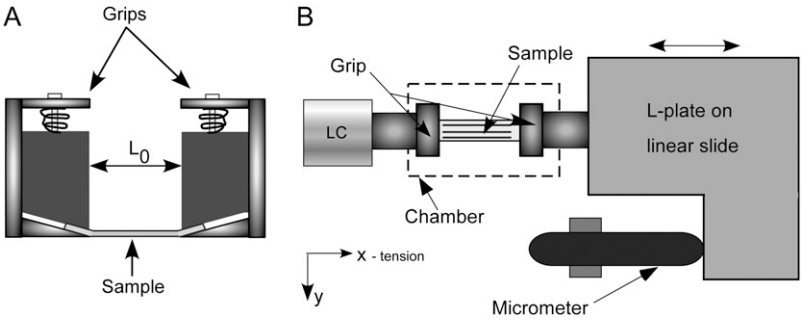

FIGURE 2 (*A*) Sample is assembled between two spring-loaded grips, and the natural grip-to-grip distance is labeled L_0. The sample-grip unit is then assembled into the deformation device (*B*) such that the predominant collagen fiber orientation is aligned with the *x* direction. The device consists of a micrometer, an L-shaped plate that is fixed on top of a linear slide, a chamber to hold fluid and allow for visualization of the sample by a microscope objective, and a load cell (LC).

within an image can be uniquely identified by the intensity pattern of a small square window of surrounding pixels, referred to as the ''subset mask'' (43,44). The displacement of this subset mask is determined by optimizing a correlation coefficient that depends on in-plane pixel displacement and displacement gradients (43,44). The accuracy of texture correlation analysis is dependent on the order of displacement gradients tracked (i.e., zeroth versus first order) and image quality (45). A two-dimensional, first-order algorithm was used (MATLAB, The MathWorks, Natick, MA) (45) to determine strain at both the macroscale and microscale in the meniscus tissue and within the cell micoenvironment.

Displacement measures determined from texture correlation analyses of the grayscale digital images of the meniscus ECM in the reference and deformed states were used to calculate two-dimensional Lagrangian strains (normal strains E_{xx}, E_{yy}, and shear strain E_{xy}) and principal strains (E_1, E_2) at the macroscale (10× FOV) and within a subset of the 40× images (window of the 40× FOV) representing the microscale and corresponding to a specific cell microenvironment. After application of the tensile displacement, some tissue regions and labeled cells translated out of plane when viewed at 40× relative to their undeformed spatial positions. For this reason, the image acquired for texture correlation analyses of displacement in the deformed state was either a two-dimensional image of a planar surface within the tissue, or a slice selected from a three-dimensional image stack (to ensure that the appropriate z-position in the macroscale FOV was analyzed). Strain in the microenvironment of a specific cell within each 40× FOV was calculated from displacement measures obtained for an image pair over a small window representing 45–75 μm centered on the cell. In preliminary analyses, the precision error for texture correlation analyses was estimated through calibration tests using consecutively acquired images of DTAF-labeled meniscus tissue in a reference and a digitally deformed state. The estimated precision errors for strain measurements were 0.0023 at 10× magnification and 0.0037 at 40× magnification, or 4.4% and 7.1% of the magnitude of a simulated applied strain, respectively. The magnitude of simulated applied strain in the preliminary calibration studies was 0.052, which represents a strain level similar to the grip strain used in these experiments. Therefore, these error estimates are appropriate for experiments completed in this study.

Calculation of STRs

To determine relationships between microscale strains in the cellular microenvironment and macroscale strains representative of the far-field tissue explant, an STR was defined (Eq. 1). Furthermore, this ratio enabled an evaluation of the hypothesis that macroscale strains would correspond in sense and magnitude to those transferred to the microscale surrounding all resident cells. For each strain component, this ratio is defined as the fraction of the median microscale strain measured in the vicinity of a cell (45–75 μm square) relative to the median strain within the 10× FOV. STRs were calculated for all two-dimensional Lagrangian strain components (e.g., STR_{xx} using E_{xx}) and also for the minimum and maximum principal strains (STR_{E1}, STR_{E2}):

$$STR_{ij} = \frac{E_{ij\_40X-cell}}{E_{ij\_10X}}. \quad (1)$$

To evaluate patterns and the extent of heterogeneity in measurements of STRs, k-means cluster analysis (46) was performed on STR measurements for all of the cells tracked in all samples. k-means clustering was completed using either one parameter (STR_{xx} or STR_{E2} value) or multiple parameters (both STR_{E1} and STR_{E2}). Cluster analysis was used to partition data for STR into distinct groups or clusters that were evaluated for detectable differences using ANOVA and Tukey's post hoc test (Statview, SAS Institute, Cary, NC) at a confidence level of 0.95. To identify potential relationships between matrix structure and strain transfer behaviors, the microenvironments assigned to each cluster were examined for their matrix descriptors, such as those described in Materials and Methods and Fig. 1.

RESULTS

ECM strains were obtained at macroscale and microscale levels, corresponding to the far-field tissue and cell microenvironments ($n = 32$ cellular regions from a total of 36 microscale fields of view tracked), in meniscal explants subjected to uniaxial tension ($n = 12$). Microscale cellular regions not included in the analysis resulted from a loss of the cellular region after deformation, significant out-of-plane rotation, or inability of the texture correlation algorithm to track displacements. To illustrate the procedures for analyzing the results, findings for macroscale and microscale Lagrangian strain components as well as the corresponding principal strain components and STR values are presented first for a single cell microenvironment within a representative meniscal tissue sample.

Experimental results for a single tissue-cell region

The displacement and macrostrain fields in the far-field tissue (i.e., 10× magnification) for a representative meniscal explant subjected to a 4.5% grip-to-grip tensile strain are shown in Fig. 3. In general, these strain fields were smooth across the image field, tensile along the direction of applied deformation, and more spatially heterogeneous in the transverse or y direction, exhibiting both tensile and compressive values (Fig. 3, *B–D*). For this explant, the median measured strain along the direction of applied deformation was $E_{xx} = 0.031$ (interquartile range (IQR) = 0.013). Although this value was moderately lower than expected based on the grip strain for this tissue sample, this result was not unexpected and may represent the potential for tissue slip from the grips, the presence of a coverslip boundary on the underside of the sample, misalignment of collagen fibers with the experimental x axis, or strain heterogeneity. The median strain in the transverse direction was $E_{yy} = -0.017$ (IQR = 0.011). Strain calculations also detected a significant nonzero shear strain with a median value of $E_{xy} = 0.020$ (IQR = 0.015), suggesting that the principal strains were not aligned with the x and y coordinate axes of the loading experiment.

The microscale displacement and strain fields measured for a cell microenvironment (window representing 68 × 45 μm) within this explant are summarized in Fig. 4. The cell appeared to be elongated along the x direction and embedded within a tissue region containing wide, aligned fibrous structures that resembled a fiber bundle. All median microscale strain components were close to zero ($E_{xx} = 0.004$, $E_{yy} = 0.007$, $E_{xy} = 0.008$), although with very large values for the IQR giving evidence of nonuniformities in strain calculations across the imaged region (IQR $E_{xx} = 0.024$, IQR $E_{yy} = 0.022$, IQR $E_{xy} = 0.032$). The resulting STRs in this example were $STR_{xx} = 0.13$ for the axial strain component, $STR_{yy} = -0.41$ for the transverse component, and $STR_{xy} = 0.4$ for the shear component.

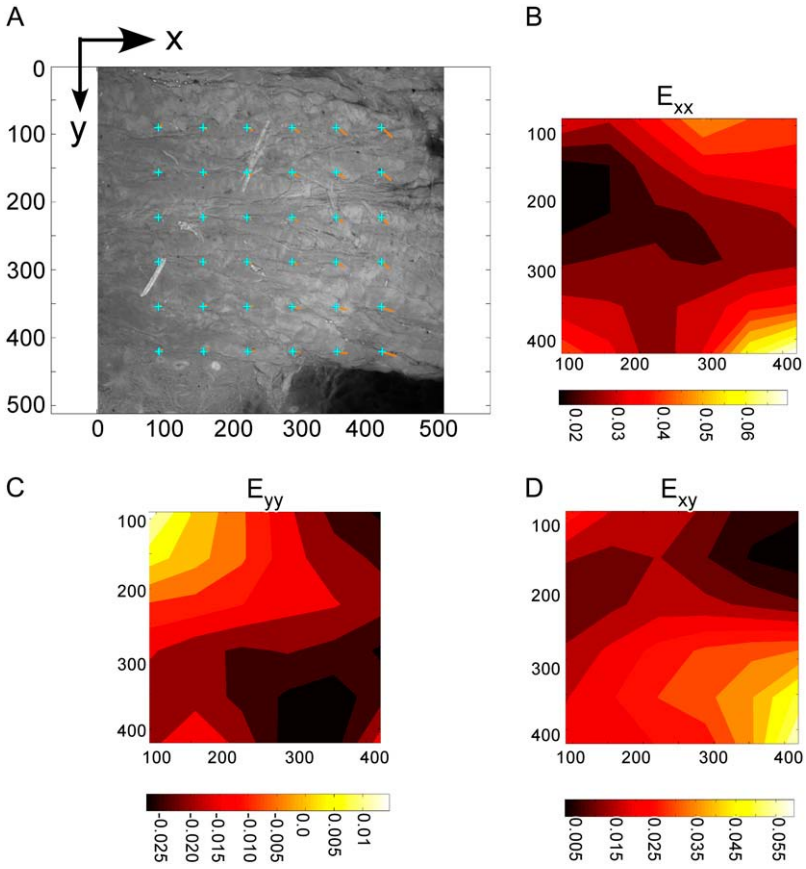

FIGURE 3 Texture correlation results for an example tissue FOV (10×). (*A*) The 10× FOV is shown with the grid of tracking points (*blue* +) and their corresponding displacements (*orange lines*). Pseudocolor plots of the strain fields for (*B*) E_{xx}, (*C*) E_{yy}, and (*D*) E_{xy} are also shown with their own color scales. The *x* and *y* directions are labeled with their pixel locations. All texture correlation measurements were made with a subset mask size of 41 pixels, a search width of 30 pixels, and a correlation coefficient tolerance of 0.02.

Principal strain analysis for this representative explant resulted in a tensile maximum principal strain (E_2) and a compressive minimum principal strain (E_1) at both macro- and microscales. The principal strain values measured at the macroscale for this representative sample were $E_1 = -0.022$ and $E_2 = 0.041$. The variability in principal strain magnitudes across the microscale or cell microenvironment was generally lower than that observed for components of the Lagrangian strain tensor at this length scale (median $E_1 = -0.012$, $E_2 = 0.023$; IQR $E_1 = 0.017$, IQR $E_2 = 0.039$). The median STR values for this example microenvironment were found to be $STR_{E1} = 0.55$ and $STR_{E2} = 0.56$.

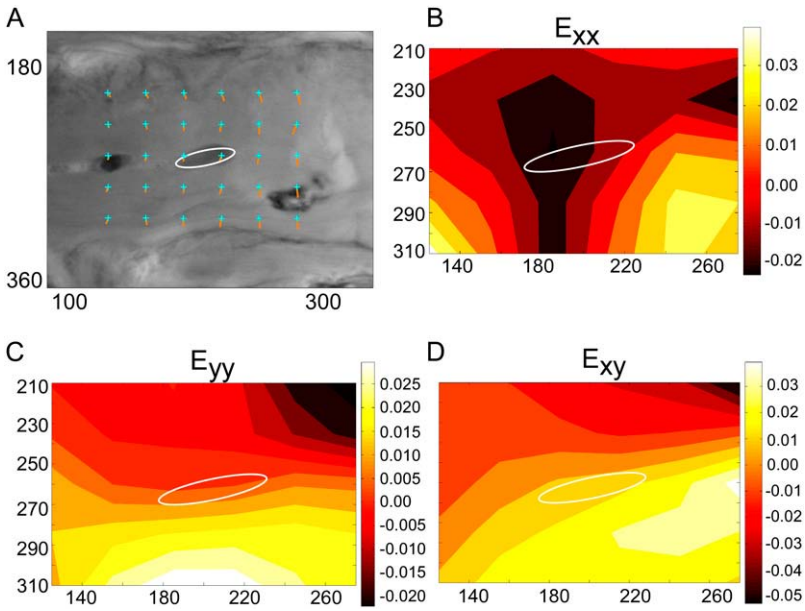

FIGURE 4 Texture correlation results for an example cellular microenvironment. (*A*) The displacements (*orange lines*) are shown for each tracking point (*blue* +) surrounding the cell, which appears as a dark oval. Pseudocolor plots of the strain fields for (*B*) E_{xx}, (*C*) E_{yy}, and (*D*) E_{xy} are also shown with their own color scales. The position of the cell appears as a white oval near the center of the field tracked. The cell is immediately surrounded by low yet nonzero magnitudes of all components of strain. The *x* and *y* directions are labeled with their pixel locations. All texture correlation measurements were made with a subset mask size of 47 pixels.

Lagrangian strain components and STRs

The histogram shown in Fig. 5 depicts the distribution of STRs determined for all cell microenvironments along the direction of applied deformation (STR_{xx}). There was evidence of significant between-sample variability, with values from –1.38 to 2.55 (IQR = 0.40–1.33 across samples). Substantial intersample variation in STRs was also present for the transverse and shear Lagrangian strain components with an IQR for STR_{yy} of −1.17 to 1.47 and an IQR for STR_{xy} of −1.28 to 1.88. These STRs for all strain components were associated with different physical interpretations that may include values close to 1 (indicating microscale strain values similar to macroscale strains), values greater than 1 (strain amplification), values <1 (strain attenuation), and negative values (indicating a change in the sense of strain, e.g., tensile macroscale strain and compressive microscale strain).

Cluster analysis using values for STR_{xx} alone demonstrated statistically significant separation of data points into distinct clusters ($p < 0.05$, ANOVA effect of cluster number, Table 1). Post hoc analysis demonstrated that each cluster was significantly different from all other clusters ($p < 0.02$, ANOVA + Tukey's post hoc test). The separation of these clusters based on STR_{xx} can be visualized graphically in Fig. 6 with sample cellular microenvironments from different clusters. These results suggest that microscale strains along the direction of applied loading may be attenuated (e.g., cluster 5), amplified (cluster 1 or 3), or close to values for those measured at the macroscale (cluster 4). The cell microenvironments within each cluster were examined for their classification by matrix descriptors to determine potential relationships between matrix features and STR_{xx} values. A majority of cell environments identified within cluster 5 (strain attenuation, centroid = 0.27, eight of 10 total microenvironments) consisted of cells that appeared to be immediately surrounded by aligned collagen fibers or fiber bundles. In contrast, microenvironments containing cells that appeared to be surrounded by homogeneously stained and organized matrix structures (seven total microenvironments) tended to exhibit STR values greater than 1, suggesting strain amplification, and were predominantly clustered into either cluster 1 (centroid = 2.34, 2/3 cells) or cluster 3 (centroid = 1.39, 4/8 cells). The remaining cell microenvironments in these clusters consisted of cells within fiber junctions and nonfibrous matrices.

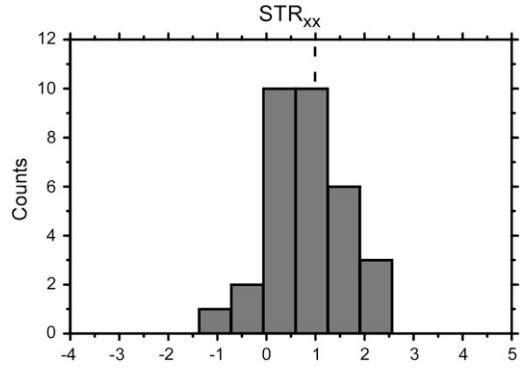

FIGURE 5 Histograms depict the count of STR values for E_{xx} in each of six bins. Each STR_{xx} value is computed as the ratio between the median strain in the cell microenvironment and the median strain across the entire 10× FOV. A dotted vertical line appears at STR = 1 to illustrate the value where strain in the cellular microenvironment is equal to that at the 10× length scale. A total of 32 cell microenvironments were included in this analysis.

TABLE 1 Results for a one-parameter *k*-means cluster analysis

Cluster number	FOV count per cluster	STR_{xx}*
1	3	2.34 (±0.2)
2	2	−0.93 (±0.64)
3	8	1.39 (±0.16)
4	8	0.92 (±0.14)
5	11	0.27 (±0.25)

The centroid or mean of each cluster is shown for each strain component (STR_{xx}). The SD of data points within each cluster is shown in parentheses. *$p < 0.05$, ANOVA with Tukey's post hoc test for differences between each cluster.

Principal strain components and STRs

The maximum principal strain, E_2, was tensile at the microscale in all of the cell microenvironments. The minimum principal strain, E_1, at the microscale was compressive in all but one of the cell microenvironments. STR values computed from these principal strains (E_1 and E_2) are depicted as histograms in Fig. 7 for all cellular environments tracked, and suggest a predominant amplification of strain from the macroscale to the microscale (mean ± SD $STR_{E1} = 2.9 \pm 3.7$, maximum compressive; and $STR_{E2} = 1.6 \pm 0.9$, maximum tensile). These data illustrate that microscale strains in the vicinity of a cell were amplified from those at the macroscale in a majority of cellular microenvironments examined (20/32 with $STR_{E2} > 1$). The STR_{E2} value for six of the remaining cellular microenvironments suggests that strains may be attenuated in the cellular microenvironment, whereas the remaining six cellular microenvironments tracked had STR_{E2} values that were close to unity. Thus, these principal strain data indicate a trend for amplified principal matrix strains in the microenvironment of meniscus cells. The fact that this trend was not evident in STR_{xx} and STRs calculated from other Lagrangian strain components may be related to effects from in-plane rotation of matrix components or distortion of the cell microenvironment that were variable across explants and microscale regions.

Cluster analysis on STRs calculated from the principal strains (either one or two components) did not reveal distinct trends for separation of STR data into clusters as compared with results obtained using STR_{xx} values. All data were identified with one cluster that represented amplification of strain at the microscale, independently of the microstructure associated with the cell tracked.

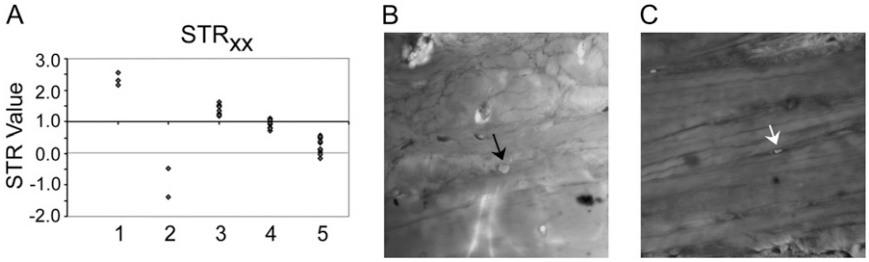

FIGURE 6 Cluster analysis revealed separation of STR_{xx} values into five distinct bins. (*A*) The STR value for each data point (*diamond*) is plotted within its cluster (numbered on the *x* axis). Panels *B* and *C* depict cells (*arrows*) within their microenvironments (ECM) for two example clusters presented as grayscale images of the fluorescent matrix and cell confocal channels. (*B*) An example homogeneously stained and organized cellular microenvironment that is localized to cluster 3. This cell microenvironment has an STR_{xx} value of 1.3. (*C*) An example cellular microenvironment that contains aligned collagen fibers, is localized to cluster 5, and has an STR_{xx} value of 0.34.

DISCUSSION

This study investigated the macroscale strain generated in a model fibrocartilaginous tissue, the meniscus, resulting from applied deformations and the transfer of the macroscale or far-field tissue strain to a microscale strain in the environment of cells. Differences in strain magnitude measured at the microscale may be due to numerous factors, including the presence of the cell as well as increased resolution of ECM structures that are complex in their organization at these small length scales, intermolecular connections, and boundary conditions along the cell-matrix interface. Results from principal strain calculations demonstrate that microscale strains are coupled to strains measured at the macroscale, or far-field tissue level, despite observations of substantial heterogeneity in measured Lagrangian strain components and tissue microstructure. The principal STR ($STR = E_{microscale}/E_{macroscale}$) for a majority of cellular regions suggested significant amplification of strains within the cell microenvironment, with values of $\sim$1.6 for the tensile component, and $\sim$2.9 for the compressive component. From finite element models of cell-matrix interactions, it is known that STR values greater than 1.0 (indicating strain amplification) are predicted for a rounded or elongated cell that is perfectly bonded to a comparatively stiff ECM (12,13,16,47,48). This is also the case reported for direct measurements of articular chondrocyte deformation in extracellular matrices in situ (21,22). Nonetheless, principal STR values close to 1.0 or $<$1.0 were also measured in this study for some meniscal cell microenvironments. These findings suggest near equivalence to or attenuation of strains at the microscale as compared to the macroscale; both effects are difficult to predict from theoretical models of cells that are mechanically more compliant than their surrounding ECM. It is likely that these observations occur because of differences in the mechanical properties of bulk explant and local tissue regions, locally varying fiber orientations (e.g., spatially varying matrix anisotropy), collagen fiber sliding, or complex fiber-matrix interactions that have been implicated in load deformation patterns for tendon (27,28) and intervertebral disc (20). Although the principal STRs in a majority of cell microenvironments were measured to have common features of strain amplification, other STR measures based on Lagrangian strain provide evidence for nonlinear deformation patterns in tissues with aligned collagen fibers.

A high degree of variability was observed for Lagrangian strain components at both macro- and microscales for all samples. This variability in meniscus strain measures, particularly at the microscale, was not surprising given the heterogeneity in matrix organization and structure at the length scale of a single cell. Spatial variability in meniscus strain measures at the macro- and microscales also resulted in a wide range of possible strain transfer mechanisms, including strain amplification, attenuation, and a change in strain sense. Strain amplification represents the common assumptions of a compliant cell in a stiff matrix with a perfectly bonded interface. Strain attenuation and a shift in strain sense may result from nonbonded cell matrix interface conditions or collagen fiber sliding, which have previously been reported for tendon (27,28) and the intervertebral disc (20). Furthermore, this variability is consistent with heterogeneous strain fields measured for isolated chondrocytes in an agarose gel under compression (49) and within single cells plated in monolayer exposed to tensile stretch (23,50) and flow-induced shear stress (51). When the principal strains are examined, however, the patterns for strain transfer appear much more uniform and consistent within and across samples,

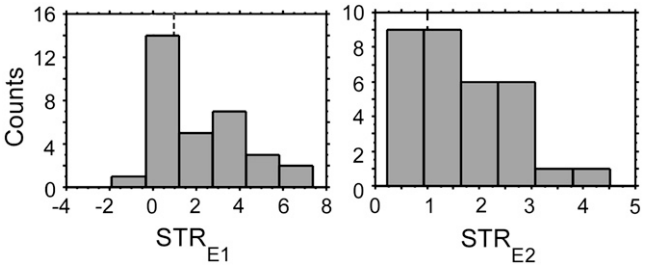

FIGURE 7 Histograms depict the count of STR values for E_1 and E_2 in each of six bins. Each STR value is computed as the ratio between the median principal strain in the cell microenvironment and the median principal strain across the entire 10$\times$ FOV. A dotted vertical line appears at STR = 1 in each plot to illustrate the value where principal strains in the cellular microenvironment is equal to that at the 10$\times$ length scale. A total of 32 cell microenvironments were included in this analysis.

suggesting that in-plane rotations of the microscale measurement region may be a common feature of applied deformation in fibrous tissues. Such in-plane rotational effects are readily associated with phenomena such as fiber sliding and fiber rotations, which have been documented in other fibrocartilaginous tissues of the intervertebral disc and ligament (19,20), but are not readily captured without principal strain analyses. In addition, these microscale rotations imply nonlinear mechanisms of deformation and a need to invoke microstructural models to describe load support in the meniscus.

Since this study sought to determine two-dimensional components of strain, great care was taken to minimize effects due to out-of-plane deformations and translations. At the tissue length scale, these effects were thought to be minimal based on the large slice thickness used for imaging sections on the confocal microscope (i.e., 30 μm in the z direction). However, for measurements of strain at the microscale, where the slice thickness was reduced by an order of magnitude, the effects may be more significant. The effect of this experimental limitation was qualitatively evaluated by acquiring multiple images of the cell microenvironment at different z positions and screening them for optimal matching with the reference image. The difference in average strain measured at the microscale for deformed images acquired at different z positions was usually less than the precision error for texture correlation. Although out-of-plane rotations would be expected to influence the magnitude of in-plane strain measured at the microscale, significant out-of plane rotations were not observed for the cells analyzed in this study, and based on preliminary experiments would have resulted in an inability of the texture correlation algorithm to determine a best-fit match for tracking points. Therefore, the resulting effect on strain component calculations and associated measures of STR was expected to be small. In general, texture correlation analysis of two-dimensional meniscus sample images yielded relatively smooth displacement and strain fields with a low precision error, and proved to be an excellent technique for gaining insight into the physical transfer of strain between the far-field tissue and cell microenvironment. An important extension of the imaging methods and strain measurements described in this study would be a three-dimensional imaging protocol and texture correlation analysis, which can be expected to yield more comprehensive measurements of strain and possibly provide additional insights into the mechanisms for strain transfer in fibrous matrices.

There is great interest in elucidating the physical processes involved in transducing mechanical stimuli from the macroscopic length scale of a tissue to those present at the microscale in the environment of single cells. Such knowledge would greatly aid our understanding of the effects of mechanical stimuli on cell phenotype and biosynthesis in physiological and pathological states. The results of this study provide new data on strain sense and magnitude within the meniscus cell microenvironment under controlled loading conditions. Findings for the strain fields measured at different length scales in meniscus tissue suggest a coordinated pattern of strain transfer from applied deformations to the microscale environment of a cell. Despite variable ECM structure and cell-matrix regions that included aligned or nonaligned cells and collagen fibers, the microscale principal strains were generally larger in magnitude and preserved the sense of strain measured at the macroscale. To our knowledge, this study provides the first reported data for multidimensional measurements of strain fields and principal strains for meniscus cells surrounded by their fibrous, native matrix that yield novel insights into the physical processes of strain transfer. Additional studies are needed to document three-dimensional strain fields in fibrous tissues to more completely determine strain transfer mechanisms and the potential role of fiber sliding, fiber-fiber interactions, fiber rotations, and other interactions in regulating mechanical stimuli in the vicinity of a cell.

We appreciate the support of Mr. Robert Nielsen and Mr. Stephen Johnson in tissue procurement.

This study was supported by National Institutes of Health grants AR047442, AR050245, AR048852, and AG015768.

REFERENCES

1. Aaron, R. K., D. M. Ciombor, S. Wang, and B. Simon. 2006. Clinical biophysics: the promotion of skeletal repair by physical forces. *Ann. N. Y. Acad. Sci.* 1068:513–531.
2. Benjamin, M., and B. Hillen. 2003. Mechanical influences on cells, tissues and organs—''mechanical morphogenesis.'' *Eur. J. Morphol.* 41:3–7.
3. AufderHeide, A. C., and K. A. Athanasiou. 2004. Mechanical stimulation toward tissue engineering of the knee meniscus. *Ann. Biomed. Eng.* 32:1161–1174.
4. Imler, S. M., A. N. Doshi, and M. E. Levenston. 2004. Combined effects of growth factors and static mechanical compression on meniscus explant biosynthesis. *Osteoarthritis Cartilage.* 12:736–744.
5. Setton, L. A., and J. Chen. 2004. Mechanobiology of the intervertebral disc and relevance to disc degeneration. *J. Bone Joint Surg. Am.* 88: 52–57.
6. Upton, M. L., J. Chen, F. Guilak, and L. A. Setton. 2003. Differential effects of static and dynamic compression on meniscal cell gene expression. *J. Orthop. Res.* 21:963–969.
7. Grodzinsky, A. J., M. E. Levenston, M. Jin, and E. H. Frank. 2000. Cartilage tissue remodeling in response to mechanical forces. *Annu. Rev. Biomed. Eng.* 2:691–713.
8. Sah, R. L., Y. Kim, J.-Y. Doong, A. Grodzinsky, A. Plaas, and J. Sandy. 1989. Biosynthetic response of cartilage explants to dynamic compression. *J. Orthop. Res.* 7:619–636.
9. Hennerbichler, A., B. Fermor, J. B. Weinberg, D. Pisetsky, and F. Guilak. 2007. Regional differences in prostaglandin E2 and nitric oxide production in the knee meniscus in response to dynamic compression. *Biochem. Biophys. Res. Commun.* 358:1047–1053.
10. Fink, C., B. Fermor, J. B. Weinberg, D. S. Pisetsky, M. A. Misukonis, and F. Guilak. 2001. The effect of dynamic mechanical compression on nitric oxide production in the meniscus. *Osteoarthritis Cartilage.* 9:481–487.
11. Alexopoulos, L. G., L. A. Setton, and F. Guilak. 2005. The biomechanical role of the chondrocyte pericellular matrix in articular cartilage. *Acta Biomater.* 1:317–325.

12. Baer, A. E., and L. A. Setton. 2000. The micromechanical environment of intervertebral disc cells: Effect of matrix anisotropy and cell geometry predicted by a linear model. *J. Biomech. Eng.* 122:245–251.

13. Guilak, F., and V. C. Mow. 2000. The mechanical environment of the chondrocyte: a biphasic finite element model of cell-matrix interactions in articular cartilage. *J. Biomech.* 33:1663–1673.

14. Gupta, T., and T. L. Haut Donahue. 2006. Role of cell location and morphology in the mechanical environment around meniscus cells. *Acta Biomater.* 2:483–492.

15. Likhitpanichkul, M., X. Guo, and V. C. Mow. 2005. The effect of matrix tension-compression nonlinearity and fixed negative charges on chondrocyte responses in cartilage. *Mol. Cell. Biomech.* 2:191–204.

16. Upton, M. L., F. Guilak, T. A. Laursen, and L. A. Setton. 2006. Finite element predictions of region-specific cell-matrix mechanics in the meniscus. *Biomech. Model. Mechanobiol.* 5:140–149.

17. Friedl, P. 2004. Dynamic imaging of cellular interactions with extracellular matrix. *Histochem. Cell Biol.* 122:183–190.

18. Pedersen, J. A., and M. A. Swartz. 2005. Mechanobiology in the third dimension. *Ann. Biomed. Eng.* 33:1469–1490.

19. Bruehlmann, S. B., P. A. Hulme, and N. A. Duncan. 2004. In situ intercellular mechanics of the bovine outer annulus fibrosus subjected to biaxial strains. *J. Biomech.* 37:223–231.

20. Bruehlmann, S. B., J. R. Matyas, and N. A. Duncan. 2004. ISSLS prize winner: collagen fibril sliding governs cell mechanics in the anulus fibrosus. *Spine.* 29:2612–2620.

21. Chahine, N. O., C. T. Hung, and G. A. Ateshian. 2007. In-situ measurements of chondrocyte deformation under transient loading. *Eur. Cell. Mater.* 13:100–111.

22. Choi, J. B., I. Youn, L. Cao, H. A. Leddy, C. L. Gilchrist, L. A. Setton, and F. Guilak. 2007. Zonal changes in the three-dimensional morphology of the chondron under compression: the relationship among cellular, pericellular, and extracellular deformation in articular cartilage. *J. Biomech.* 40:2596–2603.

23. Gilchrist, C. L., S. W. Witvoet-Braam, F. Guilak, and L. A. Setton. 2007. Measurement of intracellular strain on deformable substrates with texture correlation. *J. Biomech.* 40:786–794.

24. Guilak, F., A. Ratcliffe, and V. C. Mow. 1995. Chondrocyte deformation and local tissue strain in articular cartilage: A confocal microscopy study. *J. Orthop. Res.* 13:410–421.

25. Knight, M. M., Z. Bomzon, E. Kimmel, A. M. Sharma, D. A. Lee, and D. L. Bader. 2006. Chondrocyte deformation induces mitochondrial distortion and heterogeneous intracellular strain fields. *Biomech. Model. Mechanobiol.* 5:180–191.

26. Roeder, B. A., K. Kokini, J. P. Robinson, and S. L. Voytik-Harbin. 2004. Local, three-dimensional strain measurements within largely deformed extracellular matrix constructs. *J. Biomech. Eng.* 126:699–708.

27. Arnoczky, S. P., M. Lavagnino, J. Whallon, and A. Hoonjan. 2002. In situ cell nucleus deformation in tendons under tensile load: a morphological analysis using confocal laser microscopy. *J. Orthop. Res.* 20: 29–35.

28. Screen, H. R. C., D. A. Lee, D. L. Bader, and J. C. Shelton. 2004. An investigation into the effects of the hierarchical structure of tendon fascicles on micromechanial properties. *Proc. Inst. Mech. Eng. H J. Eng. Med.* 218:109–119.

29. Feng, H., M. Danfelter, B. Stromqvist, and D. Heinegard. 2006. Extracellular matrix in disc degeneration. *J. Bone Joint Surg. Am.* 88(Suppl 2):25–29.

30. Kambic, H. E., and C. A. McDevitt. 2005. Spatial organization of types I and II collagen in the canine meniscus. *J. Orthop. Res.* 23:142–149.

31. Adams, M. A., and D. W. L. Hukins. 1992. The extracellular matrix of the meniscus. *In* Knee Meniscus: Basic and Clinical Foundations. V. C. Mow, S. P. Arnoczky, and D. W. Jackson, editors. Raven Press, New York. 15–28.

32. McDevitt, C. A., S. Mukherjee, H. Kambic, and R. Parker. 2002. Emerging concepts of the cell biology of the meniscus. *Curr. Opin. Orthop.* 13:345–350.

33. Mow, V. C., A. Ratcliffe, K. Y. Chern, and M. A. Kelly. 1992. Structure and function relationships of the menisci of the knee. *In* Knee Meniscus: Basic and Clinical Foundations. V. Mow, S. P. Arnoczky, and D. Jackson, editors. Raven Press, New York. 37–59.

34. Upton, M. L., J. Chen, and L. A. Setton. 2006. Region-specific constitutive gene expression in the adult porcine meniscus. *J. Orthop. Res.* 24:1562–1570.

35. Valiyavettil, M., J. S. Mort, and C. A. McDevitt. 2005. The concentration, gene expression, and spatial distribution of aggrecan in canine articular cartilage, meniscus, and anterior and posterior curciate ligaments: a new molecular distinction between hyaline cartilage and fibrocartilage in the knee joint. *Connect. Tissue Res.* 46:83–91.

36. Djurasovic, M., J. W. Aldridge, R. Grumbles, M. P. Rosenwasser, D. Howell, and A. Ratcliffe. 1998. Knee joint immobilization decreases aggrecan gene expression in the meniscus. *Am. J. Sports Med.* 26:460–466.

37. Hellio Le Graverand, M. P., E. Vignon, I. G. Otterness, and D. A. Hart. 2001. Early changes in lapine menisci during osteoarthritis development Part II: Molecular alterations. *Osteoarthritis Cartilage.* 9:65–72.

38. Wildey, G. M., A. C. Billetz, J. R. Matyas, M. E. Adams, and C. A. McDevitt. 2001. Absolute concentrations of mRNA for type I and type VI collagen in the canine meniscus in normal and ACL-deficient knee joints obtained by RNAse protection assay. *J. Orthop. Res.* 19:650–658.

39. Shin, S. J., B. Fermor, J. B. Weinberg, D. S. Pisetsky, and F. Guilak. 2003. Regulation of matrix turnover in meniscal explants: role of mechanical stress, interleukin-1, and nitric oxide. *J. Appl. Physiol.* 95: 308–313.

40. Fermor, B., D. Jeffcoat, A. Hennerbichler, D. Pisetsky, J. B. Weinberg, and F. Guilak. 2004. The effects of cyclic mechanical strain and tumor necrosis factor alpha on the response of cells of the meniscus. *Osteoarthritis Cartilage.* 12:956–962.

41. Upton, M. L., A. Hennerbichler, B. Fermor, F. Guilak, J. B. Weinberg, and L. A. Setton. 2006. Biaxial strain effects on cells from the inner and outer regions of the meniscus. *Connect. Tissue Res.* 47:207–214.

42. Bay, B. K. 1995. Texture correlation: a method for the measurement of detailed strain distributions within trabecular bone. *J. Orthop. Res.* 13: 258–267.

43. Lu, H., and P. D. Cary. 2000. Deformation measurements by digital image correlation: implementation of a second-order displacement gradient. *Exp. Mech.* 40:393–400.

44. Vendroux, G., and W. G. Knauss. 1998. Submicron deformation field measurements: Part 2: improved digital image correlation. *Exp. Mech.* 38:86–92.

45. Gilchrist, C. L., J. Q. Xia, L. A. Setton, and E. W. Hsu. 2004. High-resolution determination of soft tissue deformations using MRI and first-order texture correlation. *IEEE Trans. Med. Imaging.* 23:546–553.

46. Mitchell, T. M. 1997. Machine Learning. WCB/McGraw Hill, Boston, MA.

47. Baer, A. E., T. A. Laursen, F. Guilak, and L. A. Setton. 2003. The micromechanical environment of intervertebral disc cells determined by a finite deformation, anisotropic, and, biphasic finite element model. *J. Biomech. Eng.* 125:1–11.

48. Wu, J. Z., W. Herzog, and M. Epsetin. 1999. Modeling of location- and time-dependent deformation of chondrocytes during cartilage loading. *J. Biomech.* 32:563–572.

49. Sawae, Y., J. C. Shelton, D. L. Bader, and M. M. Knight. 2004. Confocal analysis of local and cellular strains in chondrocyte-agarose constructs subjected to mechanical shear. *Ann. Biomed. Eng.* 32:860–870.

50. Wall, M. E., P. S. Weinhold, T. Siu, T. D. Brown, and A. J. Banes. 2007. Comparison of cellular strain with applied substrate strain in vitro. *J. Biomech.* 40:173–181.

51. Helmke, B. P., A. B. Rosen, and P. F. Davies. 2003. Mapping mechanical strain of an endogenous cytoskeletal network in living endothelial cells. *Biophys. J.* 84:2691–2699.